48th AIAA Aerospace Sciences Meeting Including the New Horizons Forum and Aerospace Exposition
4 - 7 January 2010, Orlando, Florida

Optical Miniaturization of a MEMS-Based Floating Element Shear Stress Sensor with Moiré Amplification

Chen, T.,[1] Mills, D.,[2] Chandrasekharan, V.,[3] Zmuda, H.,[4] and Sheplak, M.[5]
Interdisciplinary Microsystems Group, University of Florida, Gainesville, FL, 32611

A miniaturized optical package was developed for a floating-element shear stress sensor that permits the direct measurement of skin friction based on geometric Moiré interferometry. Aluminum gratings are placed on a silicon floating element and a Pyrex support structure to generate a Moiré fringe pattern, which is used to optically amplify the floating element deflections. The Moiré fringe is discretely sampled and modeled as a sinusoid. Several fringe estimation techniques are evaluated to track the phase of the Moiré fringe. Initial static characterization of the device using conventional large-scale optics indicates a shear stress sensitivity of 59 *nm/Pa* with linearity designed up to 5 *Pa*. The overall size of the optical components and packaging is significantly reduced by using an optical fiber array instead of an optical lens system to reflect light off of the Moiré fringe patterns on the shear stress sensor for optical detection.

I. Introduction

The ability to measure time-resolved shear stress is an enabling technology for aerodynamic applications, flow control and biomedical applications [1, 2]. Indirect and direct shear stress sensors have been developed for such measurements. While indirect shear stress sensors typically infer the amount of shear stress by correlating other flow related quantities, such as temperature, to shear stress, direct shear stress sensors, such as floating element based shear stress sensors, directly measure the shear stress while minimizing the disturbance in the flow. MEMS-based shear stress sensors offer high temporal bandwidth and the necessary spatial resolution to measure shear stress.

Several types of floating element MEMS shear stress sensors have been developed. The floating element transduction schemes include capacitive [3, 4] piezoresistive [5-7] and optical techniques [8, 9]. Of the three transduction sensing techniques, the optical shear stress sensor offers the potential for underwater measurement applications and high temperature shear stress measurements. Other benefits for the optical shear stress sensor include immunity from electromagnetic interference and insensitivity to pressure fluctuations when using optical techniques such as Moiré interferometry [8]. The key benefit of using an optical Moiré transduction scheme is that the mechanical motion in the floating element is amplified, effectively increasing the sensitivity of the sensor [8]. The challenge faced when using an optical sensing technique is that the size of the optical package is typically quite bulky and inappropriate for anything but benchtop measurements. The goal of this research is to minimize the size of the optical components to enable shear stress measurements in a practical real-world application.

---

[1] Graduate Research Assistant, Department of Electrical and Computer Engineering, 216 Larsen Hall, Gainesville, FL 32611-6200.
[2] Graduate Research Assistant, Department of Mechanical and Aerospace Engineering, 231 MAE-Al, Gainesville, FL 32611-6250.
[3] Research Associate, Department of Mechanical and Aerospace Engineering, 231 MAE-Al, Gainesville, FL 32611-6250.
[4] Associate Professor of Electrical and Computer Engineering, 216 Larsen Hall, Gainesville, FL 32611-6200.
[5] Professor of Mechanical and Aerospace Engineering, AIAA Associate Fellow, 231 MAE-A, Gainesville, FL 32611-6250.

Tai-An Chen, David Mills, Vijay Chandrasekharan, Henry Zmuda, and Mark Sheplak. "Optical Miniaturization of a MEMS-Based Floating Element Shear Stress Sensor with Moiré Amplification", 48th AIAA Aerospace Sciences Meeting Including the New Horizons Forum and Aerospace Exposition, Aerospace Sciences Meetings, https://doi.org/10.2514/6.2010-498

The next section describes the Moiré amplification technique used in the optical shear stress sensor. The subsequent section describes several fringe estimation techniques to monitor shifts in the Moiré fringe. An initial static calibration for the device using macro-scale optics is presented followed by a description of the miniaturized optical packaging. The results of the miniaturized optical calibration are shown in addition to a comparison of various fringe estimation techniques using the miniaturized optical data. This paper is concluded with a brief summary and suggestions for future work.

II. Moiré Transduction

The optical Moiré shear stress sensor structure consists of a silicon floating element suspended by four tethers on a silicon support structure. The silicon structure is anodic bonded to a Pyrex (Corning 7740) support structure with optical gratings patterned on both the silicon floating element and the Pyrex structure to allow backside optical transduction as shown in Figure 1a. Each set of aluminum optical gratings have a slightly different pitch that results in a Moiré fringe pattern [10] as illustrated in Figure 1b. The width of the grating is half the distance of the pitch and the duty cycle between grating width and space is 50%. The overall spatial period of the Moiré fringe pattern, G, is determined from the pitch of the gratings on the silicon floating element, g_1 and the pitch of the gratings on the Pyrex support structure g_2

$$\frac{1}{g_1} - \frac{1}{g_2} = \frac{1}{G}. \tag{1}$$

The Moiré amplification can be determined by the ratio

$$G/g_2. \tag{2}$$

The amplified displacement, Δ, of the Moiré fringe pattern is determined by

$$\Delta = \delta\left(\frac{G}{g_2}\right), \tag{3}$$

where δ is the grating or floating element displacement.

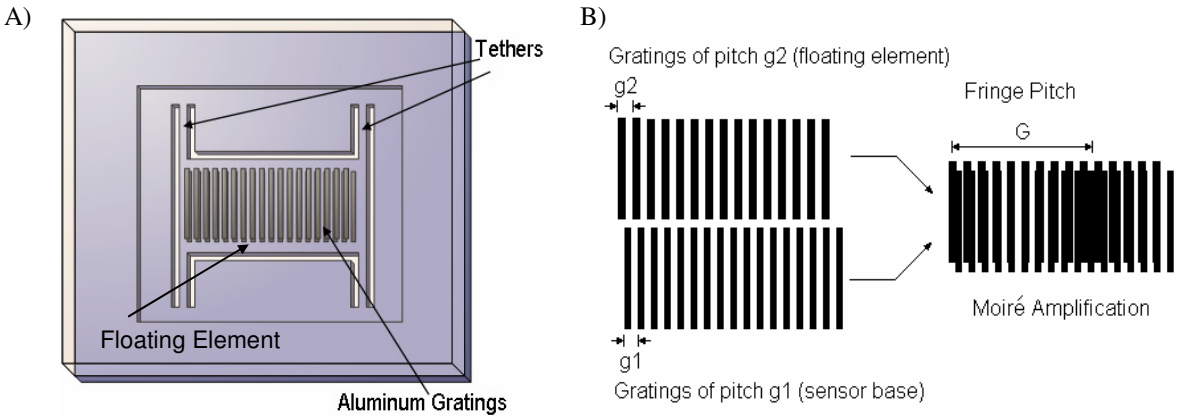

Figure 1: Optical Moiré based shear stress sensing concept. A) Top view schematic of sensor B) Graphical illustration of Moiré amplification arising from two slightly different gratings.

Due to microfabrication limitations and optimization constraints, the grating pitches, g_1 and g_2, are selected to be 9.9 μm and 10 μm respectively, which results in a Moiré amplification of 100. A whole Moiré fringe period is desirable and the width of the Moiré fringe pattern is 1 *mm*. The aluminum gratings are deposited 1 *mm* across the silicon floating element.

III. Optical Fringe Estimation Techniques

The Moiré fringe pattern generated by the sensor gratings is imaged by an array of photodetectors. Various fringe estimation techniques are investigated to process the acquired data from the detectors. The goal is to determine the amount of deflection in the floating element based on the fringe patterns, which is proportional to the imposed of shear stress. The estimation techniques used in the investigation are as follows: least squares, fast Fourier transform, cross correlation and spatial phase detection. An overview for each technique is discussed, as well as the benefits and limitations.

When the two parallel sets of optical gratings are superimposed, a Moiré fringe pattern emerges with a spatial period that is determined from the grating pitch. The repeating spatial pattern is approximately modeled by a sinusoidal function and the general form for this expression is given by,

$$y(x) = I_0 + I\sin(2\pi fx + \phi) \tag{4}$$

where y is the resulting intensity profile of the fringe pattern, I_0 is the DC offset of the sinusoid, I is the intensity amplitude, f is the spatial frequency of the Moiré fringe and is the inverse of the Moiré period $(1/G)$, x is the spatial location of the intensity measurement, and ϕ is the phase. The experimental optical fringe data is compared to this expression to track the changes in the phase to determine the spatial shift of the floating element of the device.

In this paper, the four different techniques evaluated for fringe estimation are least squares curvefit, fast Fourier transform, cross-correlation and spatial phase detection. The following sections describe how each method is applied for the fringe estimation of a sinusoid representing the Moiré pattern.

A. Least Squares Curvefit

The goal of the least-square curve-fit is to minimize the deviation between the predicted values for a sinusoidal expression and the experimental fringe data. The residuals are the errors between the predicted values and the measured values. The solution for the sinusoidal function is solved by iteratively comparing the experimental data to the predicted values until the sum of the square of the residuals is minimized [11].

The generalized form for the sinusoid, equation (4), can be linearized using the trigonometric identity

$$\sin(A+B) = \cos A\sin B + \sin A\cos B \tag{5}$$

Applying the trigonometric identity to the generalized sinusoidal equation yields

$$y = I_0 + I\left[\sin 2\pi fx\cos\phi + \cos 2\pi fx\sin\phi\right]. \tag{6}$$

Since the phase ϕ is constant, the $\sin\phi$ and $\cos\phi$ terms are rearranged with I as shown

$$y = I_0 + \underbrace{I\cos\phi}_{I_1}\sin 2\pi fx + \underbrace{I\sin\phi}_{I_2}\cos 2\pi fx. \tag{7}$$

The simplified equation is expressed as

$$y = I_0 + I_1\sin 2\pi fx + I_2\cos 2\pi fx. \tag{8}$$

The simplified equation is now in the form of a linear least squares model,

$$y = a_0 z_0 + a_1 z_1 + \ldots + a_m z_m + e. \tag{9}$$

Equation (8) is rewritten in matrix form as

$$\{y\} = [Z]\{a\} + \{e\}. \tag{10}$$

The $\{a\}$ and $[Z]$ matrix in equation (10) are expressed as

$$\{a\} = \begin{bmatrix} I_0 \\ I_1 \\ I_2 \end{bmatrix} \tag{11}$$

and

$$[Z] = \begin{bmatrix} 1 & \sin 2\pi fx_1 & \cos 2\pi fx_1 \\ 1 & \sin 2\pi fx_2 & \cos 2\pi fx_2 \\ \vdots & \vdots & \vdots \\ 1 & \sin 2\pi fx_n & \cos 2\pi fx_n \end{bmatrix}, \tag{12}$$

where n is the number of data points sampled. The sum of the square of the residuals is defined as,

$$S_r = \sum_{i=1}^{n} e^2 = \sum_{i=1}^{n} \left(y_i - \sum_{j=0}^{2} a_j Z_{ji} \right)^2 . \tag{13}$$

The sum of the square of the residuals S_r, can be rearranged into a matrix equation by taking partial derivative with respect to a and is expressed as [11]

$$\left[[Z]^T [Z] \right] \{a\} = \left\{ [Z]^T \{y\} \right\}. \tag{14}$$

The phase of the Moiré fringe displacement is now calculated using

$$\phi = \tan^{-1} \left(\frac{I_2}{I_1} \right). \tag{15}$$

B. Fast Fourier Transform

The Fast Fourier Transform (FFT) can be used as method to track the phase of a sinusoidal function. The FFT is a computationally efficient version of the Discrete Fourier Transform (DFT), which can be used to convert signals from the spatial domain into the frequency domain. Using discrete frequencies, the Fourier transform can be expressed as [12]

$$Y_k = \sum_{n=0}^{N-1} y_n e^{-j\frac{2\pi kn}{N}} , \tag{16}$$

where $k = 0, 1, 2, ..., N-1$.

In order for the FFT algorithm to work ideally, the number of samples should be in a power of 2. Furthermore, the sampled data should ideally be integer multiples of an exact signal period to avoid leakage in the power spectrum.

C. Cross-Correlation

The cross-correlation method tracks the current optical fringe by comparing the subsequent fringe shifts with an initial zero phase fringe. Respectively, the equations for the zero phase fringe and subsequent fringes is expressed as

$$y_1 = I_{01} + I_1 \sin\left(2\pi fx\right) \tag{17}$$

and

$$y_2 = I_{02} + I_2 \sin\left(2\pi fx + \phi\right). \tag{18}$$

The cross-correlation is defined as [12]

$$R_{y_1 y_2}\left(\delta\right) = E\left[y_1\left(x\right) y_2\left(x+\delta\right)\right], \tag{19}$$

where $E[\ ]$ is an expectation operator. The zero phase fringe and subsequent fringes are convolved to observe peak values in the cross-correlation. The phase shift is determined by observing the spatial shift between the peak values.

D. Spatial Phase Detection

The spatial phase detection method is a phase extraction technique based on an approach by Sajan et al. in 1989 [13]. In order to use this technique, the general sinusoid form should be modified to a cosine by introducing a $\pi/2$ phase shift, which results in the following expression.

$$y = I_0 + I\cos\left(2\pi fx + \phi - \pi/2\right). \tag{20}$$

The Fourier cosine and sine integrals can be obtained and expressed as,

$$C = \int_{-\infty}^{\infty} y\cos\left(2\pi f_0 x\right) dx \tag{21}$$

$$S = \int_{-\infty}^{\infty} y\sin\left(2\pi f_0 x\right) dx. \tag{22}$$

The cosine and sine integrals can be discretized and expressed as

$$C = \sum_{i=1}^{n} y_i \cos\left(2\pi fx\right)\Delta x \tag{23}$$

$$S = \sum_{i=1}^{n} y_i \sin\left(2\pi fx\right)\Delta x. \tag{24}$$

The phase ϕ is obtained by calculating the arctangent of C and S and is given by

$$\phi = \tan^{-1}\left(\frac{S}{C}\right). \tag{25}$$

IV. Experimental Calibration Using Large-Scaled Optics and Results

The deflection of the floating element and optical Moiré response were initially statically calibrated using large scale optics and performed in the Interdisciplinary Microsystems Laboratory at the University of Florida [8]. A digital microscope camera (Olympus DP-11) was used in the experiment to capture the Moiré pattern while the sensor was tested in a Poiseuille flow environment as shown in Figure 2. This permitted a fine resolution measurement of the Moiré fringe. The wall shear stress can be calculated by

$$\tau_w = -\frac{h}{2}\frac{\Delta p}{L}, \tag{26}$$

where Δp is the differential pressure, h is the height of the channel, and L is the distance across the differential pressure [14]. This allows the sensor to be statically calibrated in a known shear stress environment while observing the mechanical response of the sensor.

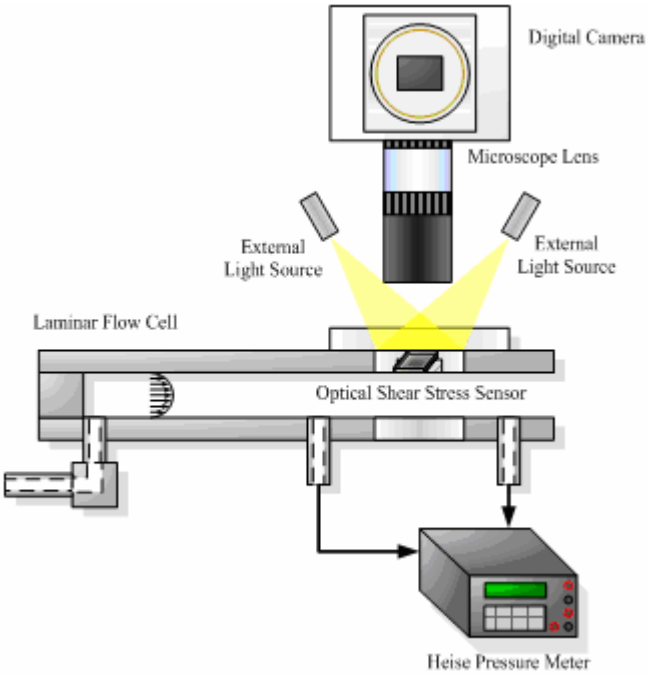

Figure 2: Experimental setup for optical shear stress sensor testing using a laminar flow cell to statically calibrate between 0 Pa to 5 Pa of shear stress.

The sensor was flush mounted on a miniature sensor chip package and then inserted into a flow plug. The flow plug containing the sensor is then mounted into a laminar flow cell with a channel height of 0.010 *inches*. A Heise pressure meter, with a 50 *in.* of H_20 module, was used to measure a pressure differential across 3 *inches*. A range of known shear stresses were generated from 0 to 5 *Pa* and the Moiré pattern was recorded at a given flow as shown in Figure 3. An external light source was used to illuminate the shear stress sensor using a reflective configuration. In the experiment, ten shear stress levels as well as a zero-flow level were observed.

The sensor range of the device used in testing was a 5 Pa, 2 kHz shear stress sensor. The floating element of the sensor has a length, width and thickness of 1000 μm, 1500 μm, and 43 μm, respectively. The tethers have a length, width and thickness of 1260 μm, 10 μm, and 43 μm, respectively. The 0.25 μm thick aluminum gratings of the sensor were set to be 9.9 μm and 10 μm in pitch, which yielded a Moiré amplification of 100.

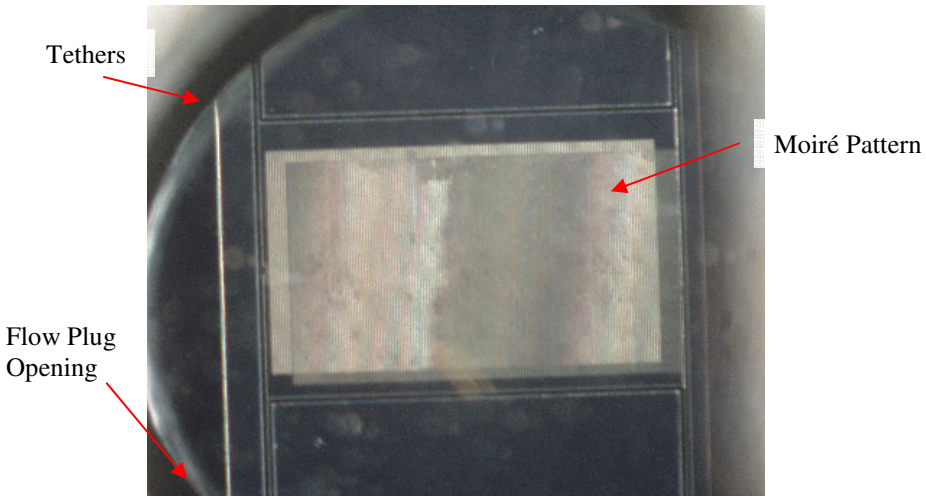

Figure 3: Photograph of the sensor using a microscope lens with 40x magnification.

At a given shear stress level, 20 averages were used to generate the mean Moiré pattern and the corresponding error bars. From the image data, around 800 *pixels* were used to represent the discretized Moiré fringe. The mean shear stress of the Moiré patterns were computed and modeled as a sinusoid, equation (4), using a least-squares curvefit algorithm in MATLAB as shown in Figure 4. During the experimental calibration procedure, mechanical vibrations between the microscope camera and the sensor were observed. The vibrations in the recorded images were taken into consideration and the effects were filtered out by using the edge of the shear stress sensor as a reference point. The reference points were used to adjust the Moiré pattern such that the vibration effects between the digital camera and the sensor were minimized.

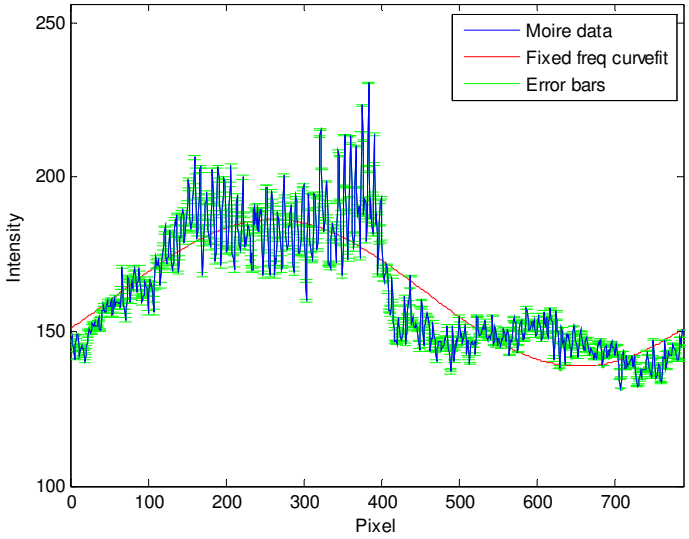

Figure 4: Sinusoidal curvefit of the Moiré pattern acquired from the sensor photographs using a least squares curvefitting algorithm.

The results of using a 5 Pa , 2 kHz shear stress sensor in the experiment yielded a sensitivity of 59 nm/Pa as shown in Figure 5. Based on the experimental static characterization, the correlation coefficient for determining the linearity in the deflection is 0.9822.

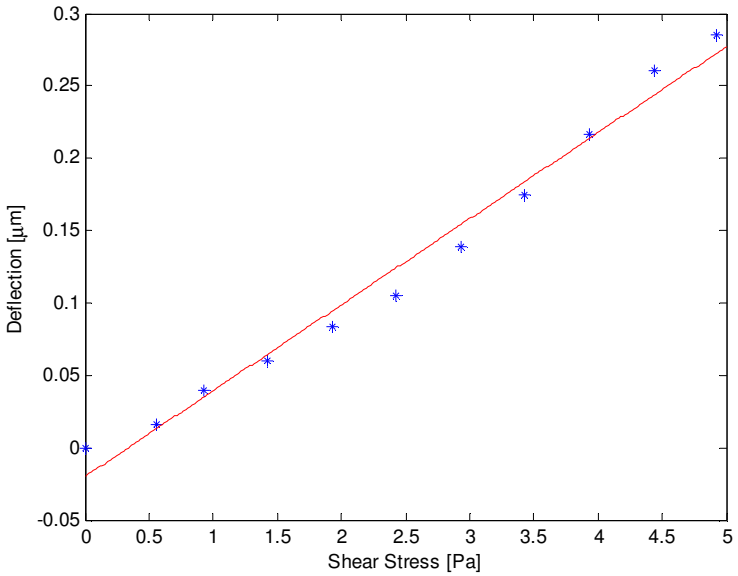

Figure 5: Floating element deflections of the shear stress sensor at given shear stress levels using least squares fringe estimation.

V. Optical Miniaturization

The optical packaging size and performance can be improved in several ways. The optical lens components of a microscope are rather large and the distance due to the depth of focus adds to packaging size. Furthermore, fixing the optoelectronics, such as the photodetectors, to the optical lens components add to the complexity of the packaging. Therefore, the optical lens components were replaced by optical fibers (Figure 6), which will enable the fibers to be attached directly to the Moiré sensor. This also enables the optoelectronic components to be located remotely from the sensor. The photodetector performance can also be improved by reducing the amount of data overhead when compared to the camera previously used. A 16-element photodiode array (Hamamatsu S4111-16Q) was selected to replace the digital camera and the number of pixels to image a Moiré pattern is reduced by at least two orders of magnitude while maintaining enough resolution for a sinusoidal curvefit. Each photodiode element in the array is spaced 1 *mm* apart and the output of all 16 photodiodes can be sampled simultaneously using a National Instruments data acquisition system (PXI-1042Q).

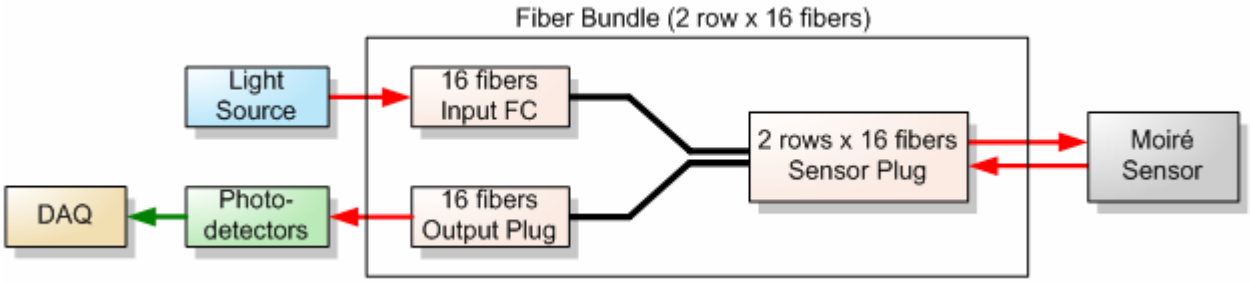

Figure 6: Overview diagram illustrating the optical setup using the fiber bundle configuration.

The custom designed optical fiber bundle was manufactured by Romack Optics (Figure 7) and consists of two rows of 16 multi-mode optical fibers, each with a 50 μm diameter core and a 65 μm diameter cladding. One row of the 16 optical fibers is used to input light from a light source towards the Moiré shear stress sensor and the second row of 16 optical fibers is used to output the light from the reflected Moiré pattern on the sensor towards the individual photodetectors. Both rows of optical fibers are packaged into a compact, 0.25 *in* x 0.25 *in* x 1.5 *in* aluminum housing that is used to observe the Moiré pattern. The spatial period of the Moiré pattern is 1 *mm* and the

two rows of optical fibers are designed to be evenly spaced across to fit one Moiré period. However, due to manufacturing issues, the resulting fibers are slightly misaligned as evidenced in the sensor plug of Figure 7. The gap between the aluminum housing and the sensor is 500 μm due to the Pyrex layer and this enables light to reflect from the input row of fibers to the output row of fibers. The individual LED light sources are coupled into the input fibers using FC connectors and the output fibers are fanned out into a second aluminum housing plug with dimensions of 0.3125 *in* x 0.75 *in* x 1.75 *in*. The fiber spacing at the output aluminum housing plug is 1 *mm* and is coupled into the 16-element photodiode array.

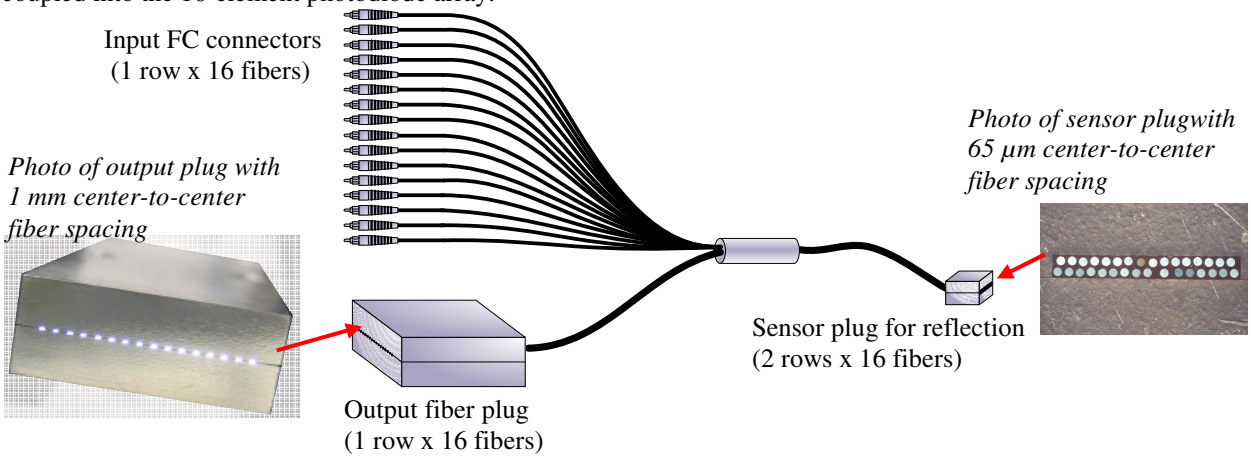

Figure 7: Drawing of the optical fiber bundle along with photographs of the fiber configuration at the sensor plug and at the output plug.

VI. Optical Test-bed Results and Discussions

An optical test bed, shown in Figure 8, was constructed to simulate the floating element Moiré sensor with the ability to mechanically control the amount of floating element deflection and the ability to exchange various optical detection setups. Two sets of aluminum gratings that match the pitch and period of the Moiré pattern on the shear stress sensor were micro-fabricated and fastened together between aluminum plates and are shown in Figure 9. A push structure is attached to a motorized stage that is driven by a linear actuator. The Newport 850G linear actuator encoder is capable of 51 *nm* resolution displacements and is used to control the amount of deflection in the simulated floating element. The fiber bundle is aligned to a single Moiré fringe pattern using an optical holder.

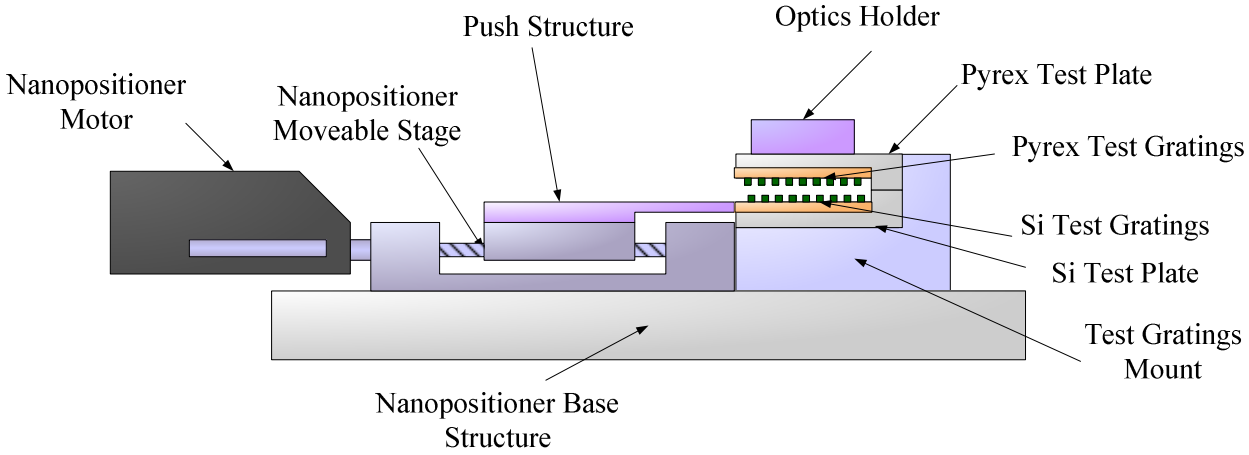

Figure 8: Drawing of the optical test-bed setup.

The width, length and thickness dimensions of the test-bed floating element are 13 *mm,* 10 *mm* and 0.5 *mm* respectively. Eight tethers are used to mechanically support the silicon floating element and each have a width of 100 μm and a length of 1000 μm . There are five regions on the floating element that contain Moiré fringe patterns.

The largest area is 7 *mm* by 7 *mm* and seven Moiré fringe periods exist within the region since g_1 and g_2 are 9.9 μm and 10 μm, respectively. The multiple Moiré periods assist with the alignment of the optical fibers and ensure that the 16 optical fibers will have an entire sinusoidal Moiré period. The smaller Moiré fringe pattern areas simulate the exact Moiré area occupied on optical shear stress sensors of various designs.

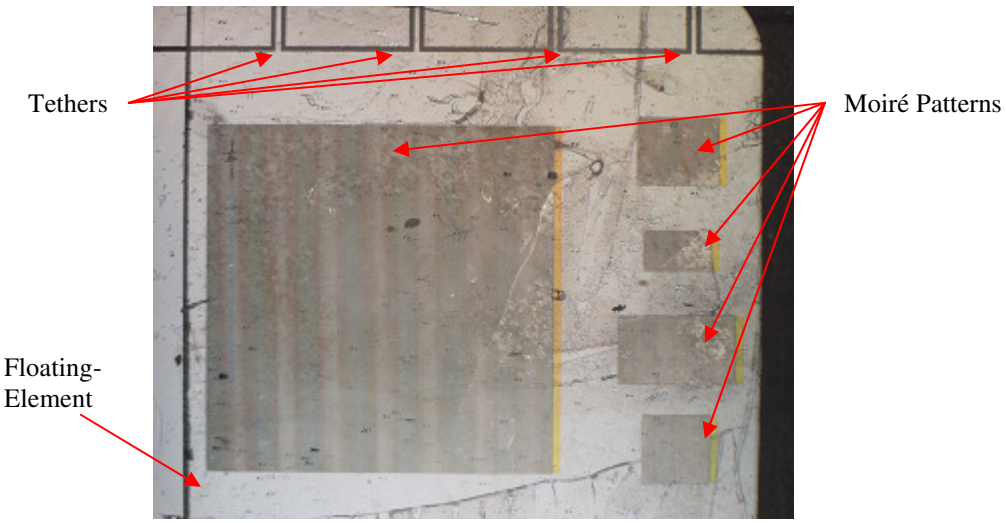

Figure 9: Photograph of the micro-fabricated floating element in the optical test-bed that is used to simulate the Moiré sensor as viewed through the Pyrex layer.

The Moiré fringe pattern was recorded at several nanopositioner displacements. Misalignment in the optical fiber from manufacturing, as well as different coupling losses with each light source cause variations in the offset, maximum and minimum values at the individual photodiodes. To compensate for this, the photodiodes were normalized by removing the mean offset and normalizing the maximum and minimum amplitude values between -1 and 1. As shown in Figure 10 and Figure 11, at each nano-positioning stage increment, a MATLAB least squares curvefit is performed on the measured 16 photodiode elements to obtain phase measurements, which is converted to displacement.

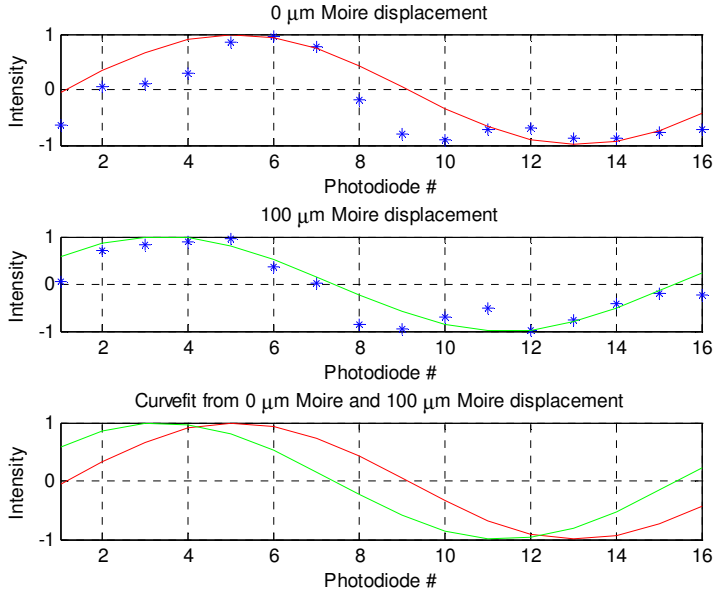

Figure 10: A least-squares curvefit on photodiode data when the Moiré fringe patterns on the test-bed floating element has been displaced: a) 0 μm b) 100 μm . A comparison of the two curvefits are shown in figure 10c).

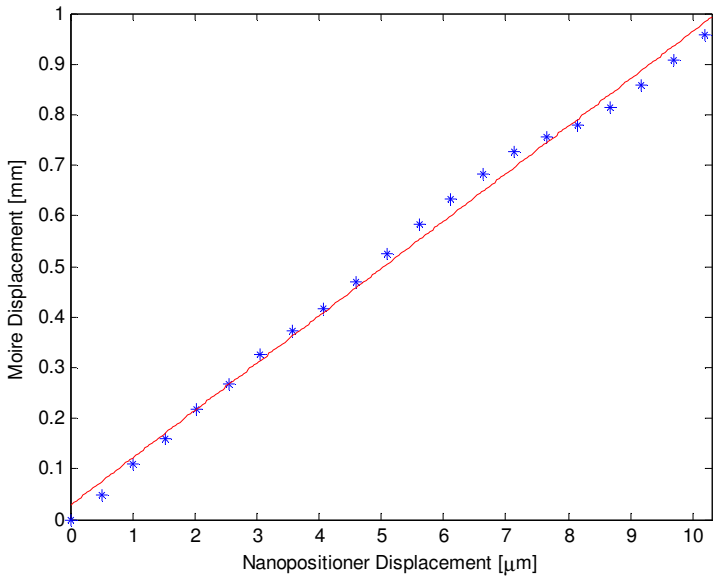

Figure 11: Moiré displacement of the simulated floating-element using the optical test-bed.

Using the test-bed, the nano-positioning stage has been displaced such that the initial Moiré phase period on the floating element will phase wrap with the next Moiré period. For such an event to occur, the Moiré pattern would have to travel 1 *mm* since the Moiré fringe period is 1 *mm*. Since the theoretical Moiré amplification is 100, for the Moiré fringe to travel 1 *mm*, that the nano-positioning stage would be displaced by 10 μm . Figure 11 shows that the slope of the line fit is 0.937 which corresponds to an experimental Moiré amplification of 93.7. The correlation coefficient for the line fit is 0.9972. The experimental fringe amplification is within the manufacturing uncertainties of the gratings.

VII. Experimental Optical Fringe Estimation Technique Comparison

Initially, the fringe shifts observed from the optical testbed using the fiber bundle were estimated using a MATLAB least squares estimation algorithm. The same testbed data is used to compare with the results of the other fringe estimation techniques. The resulting phase shifts are observed over an entire Moiré period. At each displacement, the error in the measurement for each technique is calculated using 1000 data samples. A linear fit is performed over the phase shifts and the resulting correlation coefficients are observed. The performance of the various fringe estimation algorithms is shown in Figure 12.

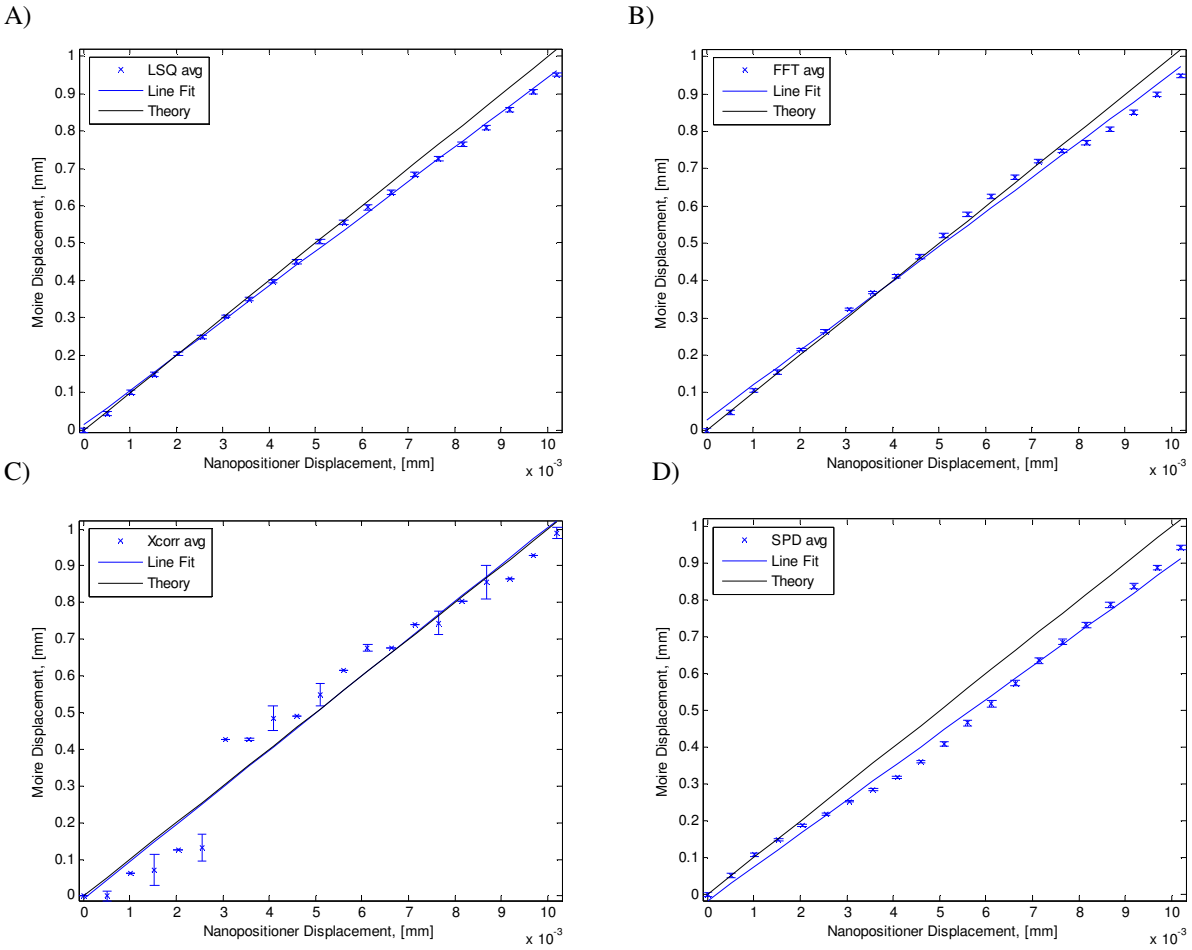

Figure 12: ***The resulting sensitivities and error bars using the A) least squares curvefit B) FFT C) cross-correlation and D) spatial phase detection fringe estimation algorithm.***

The correlation coefficients for the least squares curvefit, FFT, cross-correlation and spatial phase detection algorithms are listed in Table 1. With the exception of the cross-correlation technique, each of the algorithms offers reasonable phase estimation. Although the accuracy of various fringe estimation techniques can be improved by increasing the number of periods in the fringes, the limitations due to current manufacturing, packaging and device dimension constraints does not allow for this option. The least squares curvefit, FFT and cross-correlation have very high correlation coefficients and the slope of the line fit around 91 and 93, which corresponds to a Moiré magnification around 91 to 93. The theoretical Moiré magnification is 100. While the cross-correlation line fit has a slope of 101, the correlation coeffient is lower than the other fringe estimation techniques. While the least-squares curvefit, FFT and spatial phase detection methods show promising results, more work is needed to evaluate these techniques.

Table 1: Correlation coefficients and slopes for various algorithms

	Correlation Coefficient	Slope
Least Squares	0.9993	93.053
FFT	0.9972	92.852
Cross-Correlation	0.9824	101.312
Spatial Phase Detection	0.9965	91.097

VIII. Conclusions

A proof-of-concept miniaturized optical detection scheme for the floating-element shear stress sensor has been developed. The microfabricated optical test-bed floating element models the Moiré fringe pattern on the actual shear stress sensors and is used to test the optical fiber bundle configuration and packaging. Multiple fringe estimation techniques are evaluated to accuracy of the fringe estimation techniques. Theoretical calculations predict the Moiré period to be 1 *mm* and Moiré amplification to be 100. Optical measurements using the fiber bundle yields an experimental Moiré amplification of 93 using least squares fringe estimation.

Future work on the optical miniaturization of the MEMS-based floating element shear stress sensor is to design an optical package to mount the fiber bundle along with the device in a 2-D flow cell for calibration. Initial static calibration using a microscope yielded a sensitivity of 59 nm/Pa. The experimental sensitivity using the fiber bundle should match the sensitivity using the microscope.

References:

1. Naughton, J. and Sheplak, M., "Modern Developments in Shear-Stress Measurement." *Prog. Aero. Sci.*, Vol. 38, No. 2002, pp. 515-70.
2. Cattafesta, L. and Sheplak, M., *Actuators and Sensors*, in *Fundamentals and Applications of Modern Flow Control*. 2009, AIAA Progress in Astronautics and Aeronautics. p. 149-175.
3. Schmidt, M.A., Howe, R.T., Senturia, S.D. and Haritonidis, J.H., "Design and calibration of a microfabricated floating-element shear-stress sensor." *IEEE Tr. on Elect. Dev.*, Vol. 35, No. 6, pp. 750-57.
4. Chandrasekharan, V., Sells, J., Meloy, J., Arnold, D.P. and Sheplak, M. A metal-on-silicon differential capacitive shear stress sensor. in *Transducers 2009*, Denver, CO, USA.pp.1537-1540
5. Goldberg, H.D., Breuer, K.S. and Schmidt, M.A. A Silicon Wafer-Bonding Technology for Microfabricated Shear-Stress Sensors with Backside Contacts. in *Solid-State Sensor and Actuator Workshop*, Hilton Head, 1994.pp.111-5
6. Li, Y., et al. A laterally-implanted piezoresistive skin-friction sensor. in *Solid-State Sensors, Actuators, and Microsystems Workshop*, Hilton Head, SC.pp.304-307
7. Shajii, J., Ng, K.-Y. and Schmidt, M.A., "A microfabricated floating-element shear stress sensor using wafer-bonding technology." *J. MEMS*, Vol. 1, No. 2, 1992, pp. 89-94.
8. Horowitz, S., et al. A Wafer-Bonded, Floating Element Shear-Stress Sensor Using a Geometric Moiré Optical Transduction Technique. in *Transducers 2004*, Hilton Head, 2004.pp.13-18
9. Padmanabhan, A., Goldberg, H.D., Schmidt, M.A. and Breuer, K.S., "A Wafer-Bonded Floating-Element Shear-Stress Microsensor with Optical Position Sensing by Photodiodes." *J. MEMS*, Vol. 5, No. 1996, pp. 307-15.
10. Post, D., Han, B. and Ifju, P., *High Sensitivity Moiré*. 1994, NY: Springer. 92-105.
11. Chapra, S.C., *Applied Numerical Methods with MatLab for Engineers and Scientists*. 2008, NY: McGraw-Hill. 322-329.
12. Bendat, J.S. and Piersol, A.G., *Random Data: Analysis and Measurement Procedures*. 2000, NY: John Wiley & Sons.
13. Sajan, M.R., Tay, C.J., Shang, H.M. and Asundi, A., "Improved Spatial Phase Detection for Profilometry Using a TDI Imager." *Optics Communications*, Vol. 150, No. 1998, pp. 66-70.
14. Fox, R.W. and McDonald, A.T., *Introduction to Fluid Mechanics Fifth Edition*, ed. Wiley. 1998: John Wiley & Sons, Inc.